Signature of a pair of Majorana zero modes in superconducting gold surface states

Sujit Manna[a,b,1] (ID), Peng Wei[c,1,2], Yingming Xie[d], Kam Tuen Law[d], Patrick A. Lee[a,2], and Jagadeesh S. Moodera[a,e,f,2] (ID)

[a]Department of Physics, Massachusetts Institute of Technology, Cambridge, MA 02139; [b]Department of Physics, Indian Institute of Technology Delhi, 110 016 New Delhi, India; [c]Department of Physics and Astronomy, University of California, Riverside, CA 92521; [d]Department of Physics, Hong Kong University of Science and Technology, Hong Kong; [e]Francis Bitter Magnet Laboratory, Massachusetts Institute of Technology, Cambridge, MA 02139; and [f]Plasma Science and Fusion Center, Massachusetts Institute of Technology, Cambridge, MA 02139

Under certain conditions, a fermion in a superconductor can separate in space into two parts known as Majorana zero modes, which are immune to decoherence from local noise sources and are attractive building blocks for quantum computers. Promising experimental progress has been made to demonstrate Majorana zero modes in materials with strong spin–orbit coupling proximity coupled to superconductors. Here we report signatures of Majorana zero modes in a material platform utilizing the surface states of gold. Using scanning tunneling microscope to probe EuS islands grown on top of gold nanowires, we observe two well-separated zero-bias tunneling conductance peaks aligned along the direction of the applied magnetic field, as expected for a pair of Majorana zero modes. This platform has the advantage of having a robust energy scale and the possibility of realizing complex designs using lithographic methods.

Majorana zero mode | topological superconductor | quantum computing | Majorana bound state

Majorana zero modes (MZMs) are fermionic states, each of which is an antiparticle of itself. MZMs are required to always appear in pairs (1). Each MZM pair has the degrees of freedom of a single fermion, which is split nonlocally in space into two MZMs. The nonlocality implies that MZMs are immune to local perturbations, and hence they have been proposed as the key ingredients of topological qubits that are protected from decoherence due to local noise sources (1, 2). MZMs are predicted to exist in certain topological superconductors (TSCs). Up to now, various proposals have been made to engineer TSCs by combining conventional materials (3–9), and great progress has been made toward revealing the signatures of MZMs (10–29). Here we report the observations of signatures of MZMs in the form of zero-bias peaks (ZBP) in a platform which is based on the surface state of gold (Au). Our metal-based platform holds a number of advantages. First, there is a wealth of experience in epitaxial growth of noble metals on a variety of superconductors (30–32), as well as epitaxial growth of ferromagnetic insulators on top (33). Second, lithographic methods to produce large arrays of increasingly complex designs are well-developed. Finally, the energy scales in a metal are generally high compared with those of semiconductors. While the eventual goal of producing a topological qubit-based quantum computer is still daunting, our work opens a vision of a path forward.

Our platform is based on the Shockley surface state (SS) of Au(111) with induced superconductivity (33), as proposed theoretically several years ago (34). An important motivation of using the SS of Au(111) is its large Rashba spin–orbit coupling energy scale leading to a splitting of 110 meV (35, 36), which is several orders of magnitude larger than those in semiconductor nanowires. A schematic drawing of the needed heterostructure is shown in Fig. 1A. An Au film is grown on top of a superconductor (vanadium [V] in our case) and the bulk Au becomes superconducting due to the proximity effect. The bulk Au in turn induces a pairing gap on the SS. We have shown earlier that the SS has an energy gap of 0.38 meV,

distinct from the bulk Au gap, which is 0.61 meV (33). On top of Au we grow an epitaxial film of EuS, a ferromagnetic insulator to magnetize the Au SS via exchange coupling. We have created arrays of Au(111) wires (Fig. 1B and Fig. 2A) utilizing our epitaxially grown thin film layers and nanolithography (32, 33). The wires are 4 nm thick, ~100 nm wide or less, and microns in length as seen in Fig. 1 B and C. We emphasize that our Au(111) wires are highly crystalline with sharp edges (Fig. 1C). The scanning tunneling spectroscopy (STS) spectrum shows clearly that a hard superconducting gap is induced in the Au wire from the V underneath (see Figs. 1D, 3A, and 4D). The Au wire is homogeneously in contact with the V layer sharing a high-quality interface that is made under ultrahigh vacuum environment (Fig. 1A and see *Methods*). However, the proposal based on the SS of Au(111) has a serious limitation. The bottom of the SS band lies about 500 meV below the Fermi level (35–37). For a 100-nm-wide Au wire, this means that there are ~100 transverse subbands crossing the Fermi level. Our theory simulations show that the topological state is extremely delicate under such a condition, and it is unlikely that the MZMs have detectable signals (*SI Appendix*, section 3). Another limitation is the need for a large parallel magnetic field to
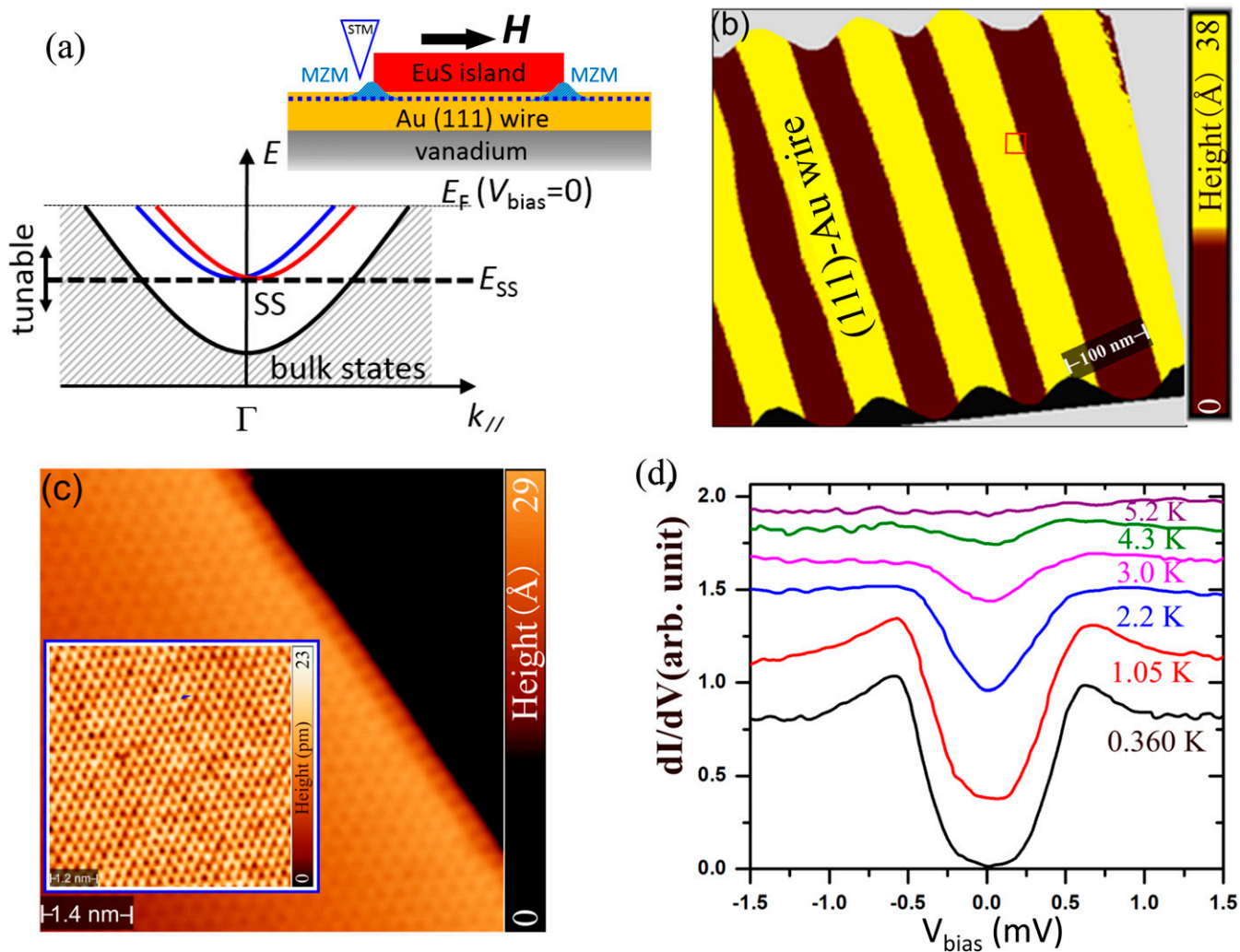
PHYSICS

Fig. 1. (*A*) Schematic of the experimental setup: Au(111) thin film nanowire proximity-coupled to a conventional superconductor V, while the EuS is grown epitaxially on top of the Au nanowires. Dotted line represents the location of the SS. An external field is applied parallel to the wire in order to drive the system into a topological superconducting state. An STM with a normal tip is used to probe the part of the MZM that leaks out from underneath the EuS island. Also shown is the schematic SS Rashba split band structure which is isolated from the projected bulk bands. The position of the bottom of the surface band (E_{SS}) can be tuned by varying the thickness of the EuS coverage. (*B*) Large-scale (650×650 nm^2) STM with constant current ($V_{sample} = 1.2$ V, $I_{set} = 55$ pA, T = 2 K) topographical scans of the nanowire network that is prepared using nanofabrication techniques. (*C*) A zoomed-in (7 nm × 7 nm) (shown by the square box in *B*) topography of Au nanowire which showed sharp interface with the underlining V film ($V_{sample} = 0.36$ V, $I_{set} = 230$ pA, T = 2 K). (*Inset*) The atomically resolved STM topography image ($V_{sample} = -150$ mV, $I_{set} = 0.6$ nA, T = 2 K) of the Au nanowire top surface, which shows the hexagonal atomic lattice of Au(111) surface. (*D*) Temperature-dependent dI/dV spectra measured on atomically resolved Au nanowire surface. The spectra are spatially averaged over a 1.5- × 1.5-nm area located at the bottom right corner of C, *Inset*. The spectra are vertically shifted and normalized by the data measured above T$_c$ (∼5 K). arb., arbitrary.

overcome the induced superconducting gap (see Figs. 1*D*, 3*A*, and 4*D*), which is much larger compared to platforms based on semiconductors with large g-factors.

We overcome the above limitations by depositing a thin layer of EuS on top of the Au wire, which has been shown to be effective in dramatically lowering the Fermi level of SS (33). In addition, EuS is a ferromagnetic insulator, known to induce sizeable magnetic exchange field in adjoining layers, thereby reducing the need for a large applied magnetic field (38–41). Fig. 2*D* shows that two monolayers (MLs) of EuS deposited on the Au wire (Fig. 2 *A–C*) is enough to shift the bottom of the SS band all the way to only ∼30 meV below the Fermi level. We ascertain this by performing a series of STS scans along the surface of an Au nanowire and comparing them with similar scans on top of a two MLs EuS island. The STS peak marked by an arrow is the signature of the band bottom of SS, characterized by a square root singularity of the

density of states. The STS peak of the pristine Au nanowire surface is at about 420 meV below the Fermi energy, consistent with the values reported by angle-resolved photoemission spectroscopy (35, 36) and STS (37). We define the chemical potential μ as the energy difference between the Fermi level and the crossing point of the Rashba bands, which lies 15 meV above the band bottom. We conclude that two MLs of EuS places the chemical potential μ to be about 15 meV. This means that for a 100-nm-wide wire only about five transverse subbands cross the Fermi level and the condition for creating MZM is much more favorable (*SI Appendix, sections 4 and 5*).

If a middle segment of the Au wire is completely covered by EuS, two MZMs are expected to emerge underneath the ends of the EuS in the presence of a magnetic field applied parallel to the wire. Unfortunately, STS probe of the Au SS through two MLs of EuS can only be done with low energy resolution. While a
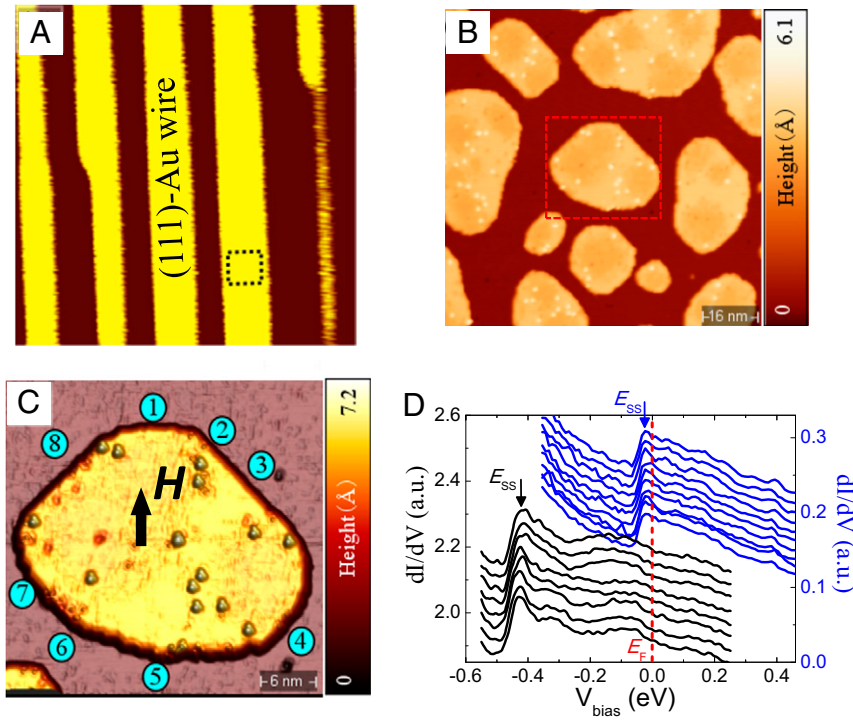
Fig. 2. (*A*) Large-scale STM topography image of the Au(111) nanowire array (similar to that in Fig. 1*B*) with two MLs of EuS deposited over it ($V_{sample} = 1.0V$, $I_{set} = 80pA$, T = 0.38 K). The size of the marked square is the same as the size of *B*. (*B*) The zoomed-in STM topography image (80×80 nm², $V_{sample} = 0.8$ V, $I_{set} = 210$ pA, T = 0.38 K) of the area denoted by a square mark in *A*. The EuS islands are clearly visible. (*C*) The further zoomed-in STM topography image (35×35 nm², $V_{sample} = 0.5$ V, $I_{set} = 0.5$ pA, T = 0.38 K) of a specific EuS island shown in *B*. (*D*) The STS (dI/dV vs. V_{bias}) spectra over large bias voltages on both bare Au(111) surface (black) and EuS island (blue). A clear shift of E_{SS} (bottom of the surface band) toward E_F is seen, which shows that the Fermi level of the Au SS underneath two MLs of EuS is ∼30 meV relative to E_{SS}. Here we emphasize the homogeneity of the sample, as demonstrated by the weak position dependence of the spectra as shown by the multiple dI/dV scans along a line. The curves are shifted vertically for clarity. a.u., arbitrary units.

continuous EuS layer can be grown to completely cover the surface of an Au wire when a thick layer of EuS is deposited, we find that EuS islands that are uniformly two MLs thick are formed when the EuS coverage is low (Fig. 2*C*). Although planar tunnel junctions can be used to tunnel through a thick EuS layer (33), as a proof of concept we focus on EuS islands and use STS for the tunneling measurements (Fig. 2*C*). In order to obtain high-resolution STS, we tunnel into the exposed Au(111) surface regions in the vicinity of an EuS island ∼2 nm away from the island edge. Fig. 1*A* shows a schematic of such measurements. If MZMs emerge underneath the EuS island, the scanning tunneling microscope (STM) tip can still couple to the MZMs due to their spatial decay (Fig. 1*A*). The decay length is found to be about 8 nm (*SI Appendix*, section 8), so 2 nm is well within the decay length.

We found ZBPs emerging inside the pairing gap when an applied magnetic field exceeds a certain value. Fig. 3 shows the tunneling spectra taken at a number of positions around an island about 30 nm wide and 25 nm long sitting on an Au nanowire (Fig. 2*C*). At zero field, the dI/dV spectra demonstrate a hard superconducting gap, which does not change regardless of the location where the STS is taken (Fig. 3*A* and 4*D*). The results demonstrate a uniformly induced superconductivity in Au(111), and the shape of the EuS island has no effect on the induced gap. With a 4.8-T magnetic field applied along the wire (called the north–south direction), a ZBP appears in positions 1, 2, and 3 near the north side of the island and near position 6 on the opposite side (Fig. 3*B*). On the other hand, anywhere in between these positions the tunneling spectra remain largely unchanged except for a small filling in the gap due to the applied magnetic field (Fig. 3*A*). To visualize the evolution of the gap and the ZBP, that is, to demonstrate the topological transition, we take the STS data with a fine scan of the magnetic field near position 6 (Fig. 2*C*). In a two-dimensional

density plot, a transition characterized by the closing of the superconducting gap and the emergence of ZBP beyond a critical field value is observed (Fig. 3*C*). The line scans (Fig. 3*D*) show that the superconducting gap evolves from a "U" to a "V" shape before the gap is filled in and the ZBP emerges after that. As we shall see, these features closely resemble the topological transition in a multimode system modeled by our theory (Fig. 6*C*).

We note that the width of the ZBP is about 0.2 meV, about a factor 2 larger than $\pi k_B T$ that is expected for the temperature of 0.38 K. The width is limited by the instrumental resolution due to the bias modulation voltage needed to achieve a signal with a sufficiently low noise (*Methods*). Therefore, it is possible that the ZBPs are due to a pair of MZMs which are hybridized to give a pair of split peaks that are not resolved. In fact, such splitting is to be expected for an island that is so small.

We next show results on a more rectangularly shaped island (60 nm × 45 nm) with an edge which overlaps the edge of the Au(111) wire as shown in Fig. 4*B*. The EuS island has excellent crystalline quality as can be seen from the atomically resolved STM image (Fig. 4*C*). We apply a magnetic field parallel to the wire and take STS measurements in the exposed Au(111) regions around the island. Again, we find uniform and fully gapped spectra at zero field (Fig. 4*D*). In a 4.8-T field, two ZBPs are observed on the opposite sides of the EuS island at the positions where the island intersects the edge of the Au wire (Fig. 4 *B* and *E*). At all other positions (labeled 2 through 7), the superconducting gap spectra remain unchanged except for a slight filling of the gap. Apparently the wavefunction corresponding to the ZBPs is strongly localized along the intersected edge of the EuS island and the Au nanowire, rather than spread out along the upper and lower edges of the EuS island. This observation is also found in our simulations discussed below, as shown in Fig.
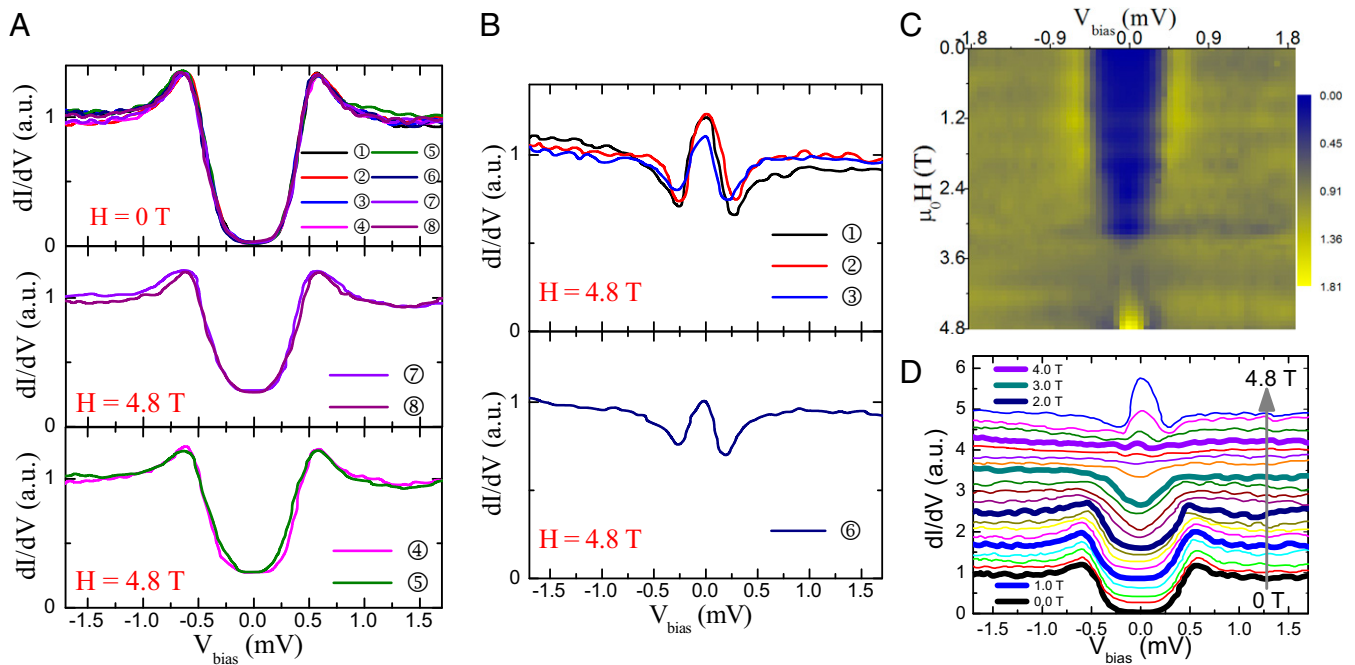
PHYSICS

Fig. 3. (*A*) The tunneling dI/dV spectra at different positions (positions 1 through 8) surrounding the EuS island acquired at T = 0.38 K as shown in Fig. 2*C*. (*Upper*) When the applied magnetic field is zero (*H* = 0T), the dI/dV spectra at all positions are fully gapped. (*Lower*) In a magnetic field (H = 4.8T) the dI/dV spectra at position 4, 5, 7, and 8 are partly filled in, but the coherence peak at the pairing gap remains intact. The direction of the magnetic field is shown in Fig. 2*C*. (*B*) Sharp ZBPs emerge at positions 1, 2, 3, and 6, consistent with the expected appearance of a pair of MZMs on opposite ends of an EuS island as defined by the magnetic field. (*C*) The two-dimensional density plot of the dI/dV data showing the topological transition of the MZM. The data are taken at a location near position 6 of the island shown in Fig. 2*C*. When the applied field increases, the superconducting gap is filled in, then it crosses over to a ZBP at sufficiently large magnetic field. (*D*) The detailed line scans of *C* are shown for various applied magnetic fields changing in small steps from 0 T to 4.8 T. The dI/dV spectra are vertically shifted for clarity. Before shifting, each spectrum is normalized to 1 at the largest V_{bias}. Starting from the bottom spectrum (field is 0 T), each vertically shifted spectrum is for a magnetic field increased in steps of 0.25 T, except for the last spectrum (the topmost one), which has an applied field of 4.8 T. In this detailed line scan plot, one can clearly see that the spectrum evolves from U- to V-shaped before completely closing, and a ZBP emerges above the filled-in gap. These data resemble our theoretical results shown in Fig. 6*C* with T = 700 mK.

5*A*. The localization of the MZM is sensitive to the local environment such as steps in the chemical potentials at the edge of the Au wire, thus accounting for the strong localization in this case.

We next study the evolution of ZBPs at positions 1 and 8 as a function of the applied magnetic field (H). At both positions the gap fills in when H is around 3.5 T (Fig. 4 *F* and *G*), which agrees well with the onset of ZBPs in the other island (Fig. 3*C*). The ZBP appears at comparable threshold magnetic fields for position 1 (at ~3.5 T) and for position 8 (at ~4 T) (Fig. 4 *F* and *G*). The slightly different threshold magnetic fields can be a result of the broad transition region as seen in Fig. 3*C*. For Fig. 3*C*, the transition takes place at around 3.5 T but has a blurred region with a span of the magnetic field of more than 0.5 T. We note that a sharp threshold field and the emergence of MZMs simultaneously at the same threshold field are not expected under our experimental conditions. There are two reasons. The first is that, unlike the quantum wire case, we are in a multimode situation. As explained below and supported by simulations shown in Fig. 6, the gap closing and the emergence of the MZM take place rather gradually due to a multitude of low-lying states near the threshold. The second reason has to do with quasi-particle poisoning due to excitations above the topological gap (Fig. 5*B*), which is defined as the energy of the lowest extended quasi-particles state. This gap closes at the topological transition and reopens at higher fields, so that just above the transition we expect a large poisoning rate Γ_p. The weight of the ZBP is reduced by the factor $\Gamma/(\Gamma + \Gamma_p)$, where Γ is the tunneling rate (42). Since Γ is very small for STM tunneling, a large reduction of the ZBP weight is expected near the topological transition at around 3.5 T. The weight gradually increases as

the topological gap reopens and Γ_p is reduced. Since Γ and Γ_p depend on the local details near the location of the MZM, the visibility and the onset magnetic field of each MZM partner is expected to have some variation, consistent with Fig. 4 *F* and *G*.

To support our interpretation, we have carried out numerical simulations on realistic models of the Au(111) wire partially covered by EuS. We perform the calculation on a square lattice with hopping and Rashba energies chosen to match the band structure of the Au SSs. We allow the chemical potential to be reduced and the effective Zeeman energy V_x to be enhanced under the EuS island. The coupling between the SS and the bulk Au states has been taken into account with a self-energy correction (*SI Appendix*, section 1). Indeed, we found that when the chemical potential under EuS is less than 30 meV, the MZMs exist over a large fraction of the chemical potential range with a relatively large gap to other subgap excitations, so that the chance of finding robust MZMs is quite high (*SI Appendix*, Fig. S2 *B* and *C*). The spectrum and the distribution of the wavefunction are shown in Fig. 5 for an island that is 60 nm × 60 nm which overlaps the edge of the Au wire. In Fig. 5*A* we see that the MZM wavefunctions are strongly localized at the corners of the intersected edge, in excellent agreement with what is seen experimentally in Fig. 4. In contrast, for a rectangularly shaped island that is in the middle of a Au wire and removed from the edge, the MZM wavefunctions are spread out along the north and south edges (*SI Appendix*, Fig. S3). It is apparent that the MZM wavefunction can be trapped by spatial inhomogeneity such as the proximity to a step in the chemical potential near the edge of the Au wire. A second point we find from the calculation is that the decay length of the MZM perpendicular to the edge
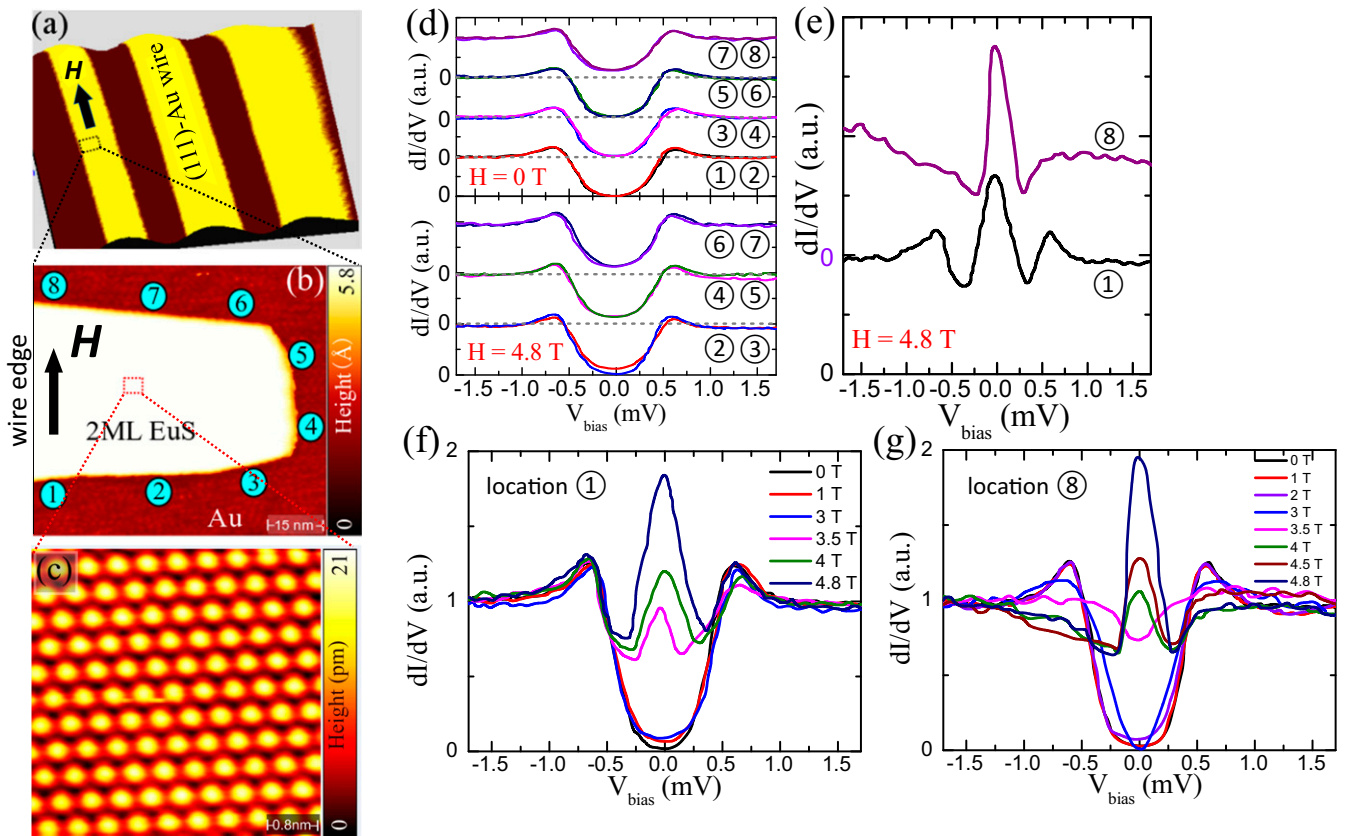
Manna et al.

Fig. 4. (*A*) The STM topography image of another Au(111) nanowire array (similar to that in Fig. 2*A*) with two MLs of EuS deposited over it (V_{sample} = 1.6 V, I_{set} = 46 pA, T = 0.38 K). The applied magnetic field is aligned with the nanowire to the best accuracy of our STM setup. (*B*) The zoomed-in STM topography image (75 × 75 nm², V_{sample} = 1 V, I_{set} = 0.5 pA) of a relatively large EuS island sitting at the edge of the Au nanowire in *A*. The island is ~40 nm long along the wire and 60 nm wide. (*C*) The atomically resolved (4 × 4 nm², V_{sample} = 120 mV, I_{set} = 600pA) EuS surface in the marked region as noted in *B*. (*D*) The comparison of the dI/dV tunneling spectra under both H = 0 T and H = 4.8 T. Dashed lines mark the zero conductance of each shifted spectrum. The spectra at all positions are gapped when H = 0 T. A slight filling in of the gap is seen at positions 2 through 7 in the 4.8-T field. (*E*) Sharp ZBP emerges for H = 4.8 T at positions 1 and 8. Curve 8 is shifted vertically by two tick marks. The zero conductance for each curve is noted with the same color as the curve. (*F* and *G*) The evolution of the dI/dV spectra at position 1 and 8 as a function of the strength of the applied field. At 3.5 T the gap is largely filled in at positions 1 and 8 simultaneously. The ZBP is visible at 3.5 T at position 1 and at 4 T at position 8. At 4-T field and above, the ZBPs at positions 1 and 8 show comparable peak heights. All of the dI/dV spectra in *D–G* are normalized to the normal-state conductance.

toward the middle of the wire is very short. This explains the surprising fact that ZBPs were observed for islands as small as 30 nm in diameter. The coherence length is short for two reasons. First, the Fermi velocity is very small because we are considering the last filled subband, which has a very small Fermi energy. Second, this situation is similar to what was observed in the Fe atomic chain (16), where the wavefunction leaks into the substrate, giving rise to a reduction of the spectral weight and the velocity, thereby reducing the effective coherence length (43). In fact, this leakage is needed to produce a surface superconducting gap close to the bulk superconducting gap Δ_B (34).

A key ingredient in the simulation is the assumption of an exchange field under the EuS in addition to the applied magnetic field. Without this, a magnetic field large enough to drive the system to a topological regime also closes the superconducting gap outside and the MZMs will be destroyed. In EuS the magnetic moment normally lies in-plane, but on certain surfaces it is known to develop a canted magnetization with a large out-of-plane component due to spin–orbit coupling (44, 45). In this case the increasing applied parallel magnetic field enhances the Zeeman field along the nanowire due to the canting of the magnetic moment. However, the precise orientation of the magnetic moment in our case is not known.

We note that much of the literature deals with the case with a single transverse mode which is relevant to the semiconductor nanowires. Here we highlight the difference with the multimode situation that is relevant to our system. To make the physics clearer, we focus on a longer island that is 60 nm × 300 nm where the energy splitting of the MZM is small and well-separated from the higher-energy states. Fig. 6*A* shows the lowest 25 eigenvalues as a function of the effective Zeeman energy V_x. We see that the gap defined by the lowest excited state closes at V_x = 1.1 Δ_B and reopens, leaving behind a pair of split MZMs. The topological gap that reopens is about 0.2 Δ_B. Note that a large number of states come down in energy as the gap closes and a large number lie above the topological gap that reopens. Consequently, the contribution of an individual state to the tunneling conductance is very small. In the single-mode case the number of states that come down as the gap closes is much fewer, depending on the sample length, and can even be a single state for short wires (*SI Appendix*, Fig. S2 *F* and *G*). As a result, the gap closing as the topological state is approached can be seen both in experiment and simulation in short nanowires (23). In contrast, in our case the lowest state that leads to gap closing as the threshold is approached contributes only a small amount to the tunneling conductance (Fig. 6*A*). Upon thermal smearing, we expect a subtle filling in of the gap which becomes V-shaped, as clearly
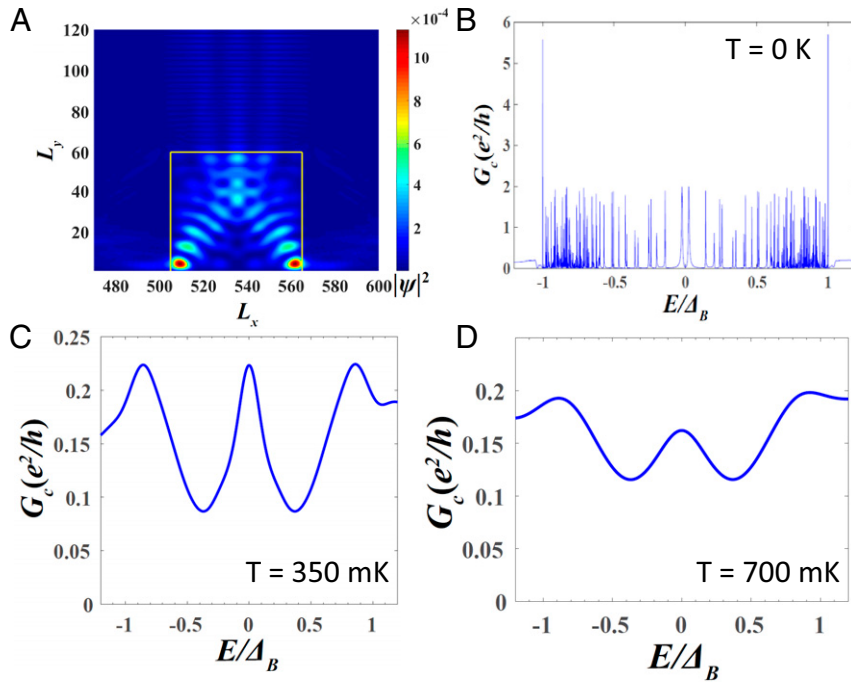
Manna et al.

Fig. 5. Simulation for a 60 nm × 60 nm island of EuS (yellow box in *A*) deposited on a 120-nm-wide Au wire. The island overlaps the lower edge. Under the island the chemical potential μ = 25 meV and the effective Zeeman energy is $V_x = 2\Delta_B$. In *A* the absolute value of the MZM wavefunction is found to be strongly localized on the edge, in agreement with the data shown in Fig. 4. The tunneling spectra at T = 0 (*B*) and 350 mK (*C*) and 700 mK (*D*) are taken at a point near the edge just outside the EuS, showing a ZBP due to an MZM. The 700-mK curve is chosen to mimic the additional instrumental broadening and can be compared with the experimental curves shown in Fig. 4*E*. The split peak near zero bias in *B* is due to the overlap of the MZM localized at opposite ends of the islands. In addition, there are in-gap states which typically start at energy of 0.1 Δ_B. Thermal smearing picks out these states as sidebands and background, as shown in *C* and *D*.

seen in Fig. 6*C*, *Right* where we show the calculated tunneling spectrum at 700 mK to simulate the additional instrumental broadening. The V-shaped spectra in the transition region also agree well with our experiment (Fig. 3*D*). With further increase of V_x beyond the threshold, the gap fills in more and eventually the MZM emerges as the topological gap opens. We emphasize that this behavior is intrinsic and not the result of disorder. We have also examined the tunneling conductance of the Au SS at a point halfway between where the ZBP appears, and just outside of the EuS island. Only the extended states contribute to these spectra. At 350 mK, we can see a slight and gradual filling in of the gap as the Zeeman field reaches and exceeds the threshold field of $V_x = 1.1 \Delta_B$ (Fig. 5*D*), in qualitative agreement with what is shown in Fig. 4*D*.

Next, we address the question of whether the ZBP we observed may be due to conventional Andreev bound states that happens to stick to zero energy. Two sources of such Andreev bound states have been discussed depending on whether disorder is present. In the absence of disorder, it has been pointed out that if the end of the wire is subject to a smooth potential, even in the non-topological region a pair of MZMs are often found near the end that are weakly hybridized with each other (46–49). One of these could couple strongly to the outside lead and the tunneling conductance resembles that of a true MZM. The reason for the lack of hybridization is that the two states may have different spins or momenta and are therefore almost orthogonal (48, 49). Such smooth potentials are generic in the semiconductor wire setup because the tunnel barrier is created by gating. In our case, the wire and the island terminate abruptly on an atomic scale and the tunnel barrier is via an STM tip. Therefore, we do not expect this mechanism to be applicable in our system, and indeed we do not see any sign of such false signals in our simulations.

A second source of false signal is that disorder potential may accidentally produce a localized Andreev bound state that happens to have energy near zero. However, such a mechanism usually requires fine-tuning of the parameters. Furthermore, it is equally likely to find such a localized state anywhere along the boundary of the island. This is in contrast to our findings because our ZBPs are aligned with the applied magnetic field and we see no sign of in-gap peaks in zero or finite field anywhere else. Finally, there is no reason why these Andreev bound states will appear at two areas on opposite sides of the same island at a similar magnetic field. In this connection we mention that the appearance of ZBPs in the EuS islands is not a rare occurrence. We have studied about 60 islands under varying experimental conditions which are sometimes not ideal in terms of STM stability. On 20 of these islands we found ZBPs which are always located either near the north or south shore with respect to the magnetic field. We also note that the spectra we see are either fully gapped or exhibit ZBPs and we never find split peaks that may be associated with Andreev bound states. Out of the 20 we saw a pair of ZBPs at opposite ends on four islands, even though in many cases we simply did not explore all the way around the island. In any event, since we do not control the chemical potential, we expect to find MZM less than 50% of the time based on our simulations, consistent with our finding.

Our simulation also found that an EuS island in the middle of a wider Au wire and away from the edges can also support MZMs, even though the wavefunction is more spread out along the edge of the island (*SI Appendix*, Fig. S3) and thus will be harder to detect with STM. We believe this explains the observation of ZBP localized on the edges of the island shown in Figs. 2 and 3. Importantly, this observation opens the door to the possibility of depositing EuS wires on a large area of Au which will allow even greater freedom in designing more complicated structures toward MZMs based
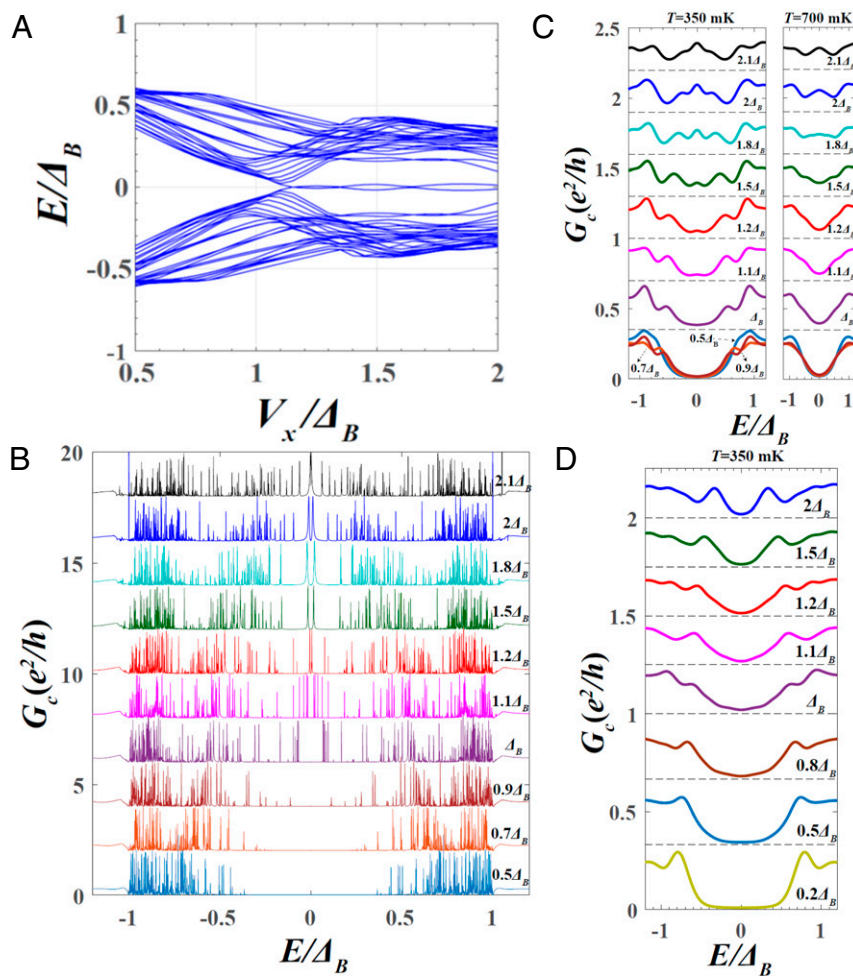
Manna et al.

Fig. 6. Simulations for a 60-nm × 300-nm island of EuS that overlaps the edge of a 120-nm-wide Au wire. (*A*) The lowest 25 eigenvalues plotted vs. the effective Zeeman energy V_x. The gap closes near $V_x = 1.1\Delta_B$ and reopens to a topological gap of about $0.2\Delta_B$. In *B* and *C* the tunneling spectra taken near the edge just outside the EuS are shown at T = 0, 350 mK and 700 mK. By looking at the T = 0 spectra in *B* we can follow the gap closing as V_x approaches the threshold. The lowest excited state carries a very small weight and is hardly visible. Above the threshold the MZM appears as a double peak split by the overlap in a finite size island. At the same time, the topological gap develops, increasing to $0.2\Delta_B$ consistent with *A*. However, a large number of states appear above the topological gap. Further examination shows that some of these states are extended, while others are localized near the ends of the wires, with a wavefunction very similar to that of the MZM. We interpret these states as "Majorana descendants," a feature of the multiband system as detailed in *SI Appendix*. Upon thermal averaging, we see in *C* that at 350 mK the gap closing is indicated by a rather subtle filling in of the gap and the MZM is gradually becoming visible above the threshold effective Zeeman field. The combination of extended states and Majorana descendants give rise to the sidebands of the MZM peak. (*C, Right*) The 700-mK curves simulate the effect of additional instrumental broadening and can be compared with the measurements shown in Fig. 4 *F* and *G*. (*D*) The tunneling spectra taken at a point at the middle of the wire just outside the EuS boundary. Only the extended states contribute. Note that the gap closing and reopening is hardly observable and is consistent with what is seen in Fig. 4*D*, *Lower*.

topological qubits. Obviously, this is something we plan to explore in the future.

The Au SS platform has a high intrinsic Rashba scale and there is room for further improvement. In the future, by going to planar tunneling an order-of-magnitude reduction in temperature and better energy resolution should be possible. A larger magnetic field can be applied which allows us to utilize superconductors with large gaps, resulting in larger topological gaps. Any coherent manipulation of MZMs requires the topological gap to be much larger than temperature. The Au SS platform holds a lot of promise toward this goal.

The Au/EuS system is amenable to flexible nanofabrication methods. For example, a single topological qubit can be constructed out of two or more wires that are cross-linked, forming "tetrons" or "hexons" that have been proposed to be building blocks of quantum computing circuits (50, 51). An array of such objects can be constructed without too much difficulty (*SI Appendix*, *section 7*). In particular, instead of braiding by physically

moving MZMs, a measurement-based topological qubit design using a purely superconducting circuit is well-suited with our Au/EuS system (52).

In conclusion, we have found signatures of MZM pairs on a superconducting Au surface as theory predicted. The Au/EuS platform has the advantage of having a robust energy scale and the potential for fabricating a large-scale network. This platform offers a plausible path, though still an extremely challenging one, toward topological quantum computing.

Methods

The heterostructures of thin film V(20 nm)/Au(4 nm) are grown in a custom-built molecular beam epitaxy system with a base vacuum ~3.7×10^{-10} torr. The growth and characterizations follow procedures similar to those we reported before (32, 33). Au nanowires, or nanoribbons, with a thickness of 4 nm and a wire width around 100 nm (or less) are fabricated after the growth of Au/V heterostructures. The nanowires are sculptured out of the wafer-scale Au thin film by following a standard e-beam lithography and an Ar ion milling process.

Manna et al.

During the nanofabrications, the surface of the superconductor V is protected in situ using a custom-built high vacuum system (base vacuum 10^{-8} torr) that combines both the ion milling and thin film evaporation sources, thereby guaranteeing the high quality of the superconductor V. Any shape of nanowire, or a network of nanowires, can be designed by standard e-beam lithography software and fabricated following such an approach (*SI Appendix*, section 7). The surfaces of Au nanowires fabricated in this way are ultraclean, as seen by the atomic resolution images of the STM (Fig. 1). A postgrowth of EuS magnetic insulator is carried out in a high vacuum system with a base vacuum $\sim 10^{-8}$ torr. The EuS growth, from islands to a continuous layer, on Au(111) surface is controllable by varying the EuS thickness as described before (33). EuS islands are chosen here to facilitate the STM measurements, because the EuS thick films are too insulating. The STM and STS experiments are performed in an ultrahigh-vacuum custom-assembled STM with an RHK PanScan head integrated in a Janis 300 mK He3 cryostat with a 5-T vector magnet. The STM is equipped with a rotating flange that allows a precise rotation of the scanning head with respect to the magnet of the cryostat, allowing us to align the applied magnetic field with the Au nanowire. Tunneling spectroscopy measurements were taken using a standard lock-in technique at 937-Hz frequency and bias modulation voltages of $V_{mod} = 80$ to 120 μV (rms value). The STM tips used were home-made, either chemically etched bulk W tips or commercial bulk PtIr tips.

1. A. Y. Kitaev, Unpaired Majorana fermions in quantum wires. *Phys. Uspekhi* **44**, 131–136 (2001).
2. A. Y. Kitaev, Fault-tolerant quantum computation by anyons. *Ann. Phys.* **303**, 2–30 (2003).
3. L. Fu, C. L. Kane, Superconducting proximity effect and majorana fermions at the surface of a topological insulator. *Phys. Rev. Lett.* **100**, 096407 (2008).
4. P. A. Lee, Proposal for creating a spin-polarized px+ipy State and majorana fermions. arXiv:0907.2681 (15 July 2009).
5. J. D. Sau, R. M. Lutchyn, S. Tewari, S. Das Sarma, Generic new platform for topological quantum computation using semiconductor heterostructures. *Phys. Rev. Lett.* **104**, 040502 (2010).
6. R. M. Lutchyn, J. D. Sau, S. Das Sarma, Majorana fermions and a topological phase transition in semiconductor-superconductor heterostructures. *Phys. Rev. Lett.* **105**, 077001 (2010).
7. Y. Oreg, G. Refael, F. von Oppen, Helical liquids and Majorana bound states in quantum wires. *Phys. Rev. Lett.* **105**, 177002 (2010).
8. J. Alicea, New directions in the pursuit of Majorana fermions in solid state systems. *Rep. Prog. Phys.* **75**, 076501 (2012).
9. C. W. J. Beenakker, Search for Majorana fermions in superconductors. *Annu. Rev. Condens. Matter Phys.* **4**, 113–136 (2013).
10. V. Mourik *et al.*, Signatures of Majorana fermions in hybrid superconductor-semiconductor nanowire devices. *Science* **336**, 1003–1007 (2012).
11. L. P. Rokhinson, X. Liu, J. K. Furdyna, The fractional a.c. Josephson effect in a semiconductor-superconductor nanowire as a signature of Majorana particles. *Nat. Phys.* **8**, 795–799 (2012).
12. J. R. Williams *et al.*, Unconventional Josephson effect in hybrid superconductor-topological insulator devices. *Phys. Rev. Lett.* **109**, 056803 (2012).
13. A. Das *et al.*, Zero-bias peaks and splitting in an Al-InAs nanowire topological superconductor as a signature of Majorana fermions. *Nat. Phys.* **8**, 887–895 (2012).
14. M. T. Deng *et al.*, Anomalous zero-bias conductance peak in a Nb-InSb nanowire-Nb hybrid device. *Nano Lett.* **12**, 6414–6419 (2012).
15. A. D. K. Finck, D. J. Van Harlingen, P. K. Mohseni, K. Jung, X. Li, Anomalous modulation of a zero-bias peak in a hybrid nanowire-superconductor device. *Phys. Rev. Lett.* **110**, 126406 (2013).
16. S. Nadj-Perge *et al.*, Topological matter. Observation of Majorana fermions in ferromagnetic atomic chains on a superconductor. *Science* **346**, 602–607 (2014).
17. S. M. Albrecht *et al.*, Exponential protection of zero modes in Majorana islands. *Nature* **531**, 206–209 (2016).
18. H.-H. Sun *et al.*, Majorana zero mode detected with spin selective andreev reflection in the vortex of a topological superconductor. *Phys. Rev. Lett.* **116**, 257003 (2016).
19. M. T. Deng *et al.*, Majorana bound state in a coupled quantum-dot hybrid-nanowire system. *Science* **354**, 1557–1562 (2016).
20. Q. L. He *et al.*, Chiral Majorana fermion modes in a quantum anomalous Hall insulator-superconductor structure. *Science* **357**, 294–299 (2017).
21. B. E. Feldman *et al.*, High-resolution studies of the Majorana atomic chain platform. *Nat. Phys.* **13**, 286–291 (2017).
22. S. Jeon *et al.*, Distinguishing a Majorana zero mode using spin-resolved measurements. *Science* **358**, 772–776 (2017).
23. H. Zhang *et al.*, Quantized Majorana conductance. *Nature* **556**, 74–79 (2018).
24. D. Wang *et al.*, Evidence for Majorana bound states in an iron-based superconductor. *Science* **362**, 333–335 (2018).
25. H. Ren *et al.*, Topological superconductivity in a phase-controlled Josephson junction. *Nature* **569**, 93–98 (2019).
26. B. Jäck *et al.*, Observation of a Majorana zero mode in a topologically protected edge channel. *Science* **364**, 1255–1259 (2019).
27. A. Fornieri *et al.*, Evidence of topological superconductivity in planar Josephson junctions. *Nature* **569**, 89–92 (2019).
28. M. M. Desjardins *et al.*, Synthetic spin-orbit interaction for Majorana devices. *Nat. Mater.* **18**, 1060–1064 (2019).
29. G. C. Ménard *et al.*, Isolated pairs of Majorana zero modes in a disordered superconducting lead monolayer. *Nat. Commun.* **10**, 2587 (2019).
30. G. Kästle *et al.*, Growth of thin, flat, epitaxial (111) oriented gold films on c-cut sapphire. *Surf. Sci.* **498**, 168–174 (2002).
31. T. Tomanic, M. Schackert, W. Wulfhekel, C. Sürgers, H. v. Löhneysen, Two-band superconductivity of bulk and surface states in Ag thin films on Nb. *Phys. Rev. B* **94**, 220503 (2016).
32. P. Wei, F. Katmis, C.-Z. Chang, J. S. Moodera, Induced superconductivity and engineered Josephson tunneling devices in epitaxial (111)-oriented gold/vanadium heterostructures. *Nano Lett.* **16**, 2714–2719 (2016).
33. P. Wei, S. Manna, M. Eich, P. Lee, J. Moodera, Superconductivity in the surface state of noble metal gold and its Fermi level tuning by EuS dielectric. *Phys. Rev. Lett.* **122**, 247002 (2019).
34. A. C. Potter, P. A. Lee, Topological superconductivity and Majorana fermions in metallic surface states. *Phys. Rev. B Condens. Matter Mater. Phys.* **85**, 094516 (2012).
35. S. LaShell, B. A. McDougall, E. Jensen, Spin splitting of an Au(111) surface state band observed with angle resolved photoelectron spectroscopy. *Phys. Rev. Lett.* **77**, 3419–3422 (1996).
36. G. Nicolay, F. Reinert, S. Hufner, P. Blaha, Spin-orbit splitting of the L-gap surface state on Au(111) and Ag(111). *Phys. Rev. B* **65**, 033407 (2001).
37. J. Kliewer *et al.*, Dimensionality effects in the lifetime of surface states. *Science* **288**, 1399–1402 (2000).
38. J. S. Moodera, T. S. Santos, T. Nagahama, The phenomena of spin-filter tunnelling. *J. Phys. Condens. Matter* **19**, 165202 (2007).
39. G.-X. Miao, J. S. Moodera, Spin manipulation with magnetic semiconductor barriers. *Phys. Chem. Chem. Phys.* **17**, 751–761 (2015).
40. B. Li *et al.*, Superconducting spin switch with infinite magnetoresistance induced by an internal exchange field. *Phys. Rev. Lett.* **110**, 097001 (2013).
41. P. Wei *et al.*, Strong interfacial exchange field in the graphene/EuS heterostructure. *Nat. Mater.* **15**, 711–716 (2016).
42. J. R. Colbert, P. A. Lee, Proposal to measure the quasiparticle poisoning time of Majorana bound states. *Phys. Rev. B* **89**, 140505 (2014).
43. Y. Peng, F. Pientka, L. I. Glazman, F. von Oppen, Strong localization of Majorana end States in chains of magnetic adatoms. *Phys. Rev. Lett.* **114**, 106801 (2015).
44. P. Wei *et al.*, Exchange-coupling-induced symmetry breaking in topological insulators. *Phys. Rev. Lett.* **110**, 186807 (2013).
45. F. Katmis *et al.*, A high-temperature ferromagnetic topological insulating phase by proximity coupling. *Nature* **533**, 513–516 (2016).
46. G. Kells, D. Meidan, P. W. Brouwer, Near-zero-energy end states in topologically trivial spin-orbit coupled superconducting nanowires with a smooth confinement. *Phys. Rev. B* **86**, 100503 (2012).
47. E. Prada, P. San-Jose, R. Aguado, Transport spectroscopy of N S nanowire junctions with Majorana fermions. *Phys. Rev. B* **86**, 180503 (2012).
48. T. D. Stanescu, S. Tewari, Illustrated guide to robust low-energy Andreev bound states in semiconductor-superconductor heterostructures: Importance of partial separation of component Majorana bound states. arXiv:1811.02557 (6 November 2018).
49. A. Vuik, B. Nijholt, A. R. Akhmerov, M. Wimmer, Reproducing topological properties with quasi-Majorana states. arXiv:1806.02801 (7 June 2018).
50. T. Karzig *et al.*, Scalable designs for quasiparticle-poisoning-protected topological quantum computation with Majorana zero modes. *Phys. Rev. B* **95**, 235305 (2017).
51. D. Litinski, F. von Oppen, Quantum computing with Majorana fermion codes. *Phys. Rev. B* **97**, 205404 (2018).
52. C. Schrade, L. Fu, Majorana superconducting qubit. *Phys. Rev. Lett.* **121**, 267002 (2018).